Inorg. Chem. **2008**, *47*, 8687−8695

Mössbauer, Electron Paramagnetic Resonance, and Theoretical Study of a High-Spin, Four-Coordinate Fe(II) Diketiminate Complex

Sebastian A. Stoian,[†] Jeremy M. Smith,[‡] Patrick L. Holland,[‡] Eckard Münck,*[,†] and Emile L. Bominaar*[,†]

Department of Chemistry, Carnegie Mellon University, Pittsburgh, Pennsylvania 15213, and Department of Chemistry, University of Rochester, Rochester, New York 14267

Received March 12, 2008

The iron(II) complex $LFeCl_2Li(THF)_2$ (L = β-diketiminate), **1**, has been studied with variable-temperature, variable-field Mössbauer spectroscopy and parallel mode electron paramagnetic resonance (EPR) spectroscopy in both solution and the solid state. In zero applied field the 4.2 K Mössbauer spectrum exhibits an isomer shift $\delta = 0.90$ mm/s and quadrupole splitting $\Delta E_Q = 2.4$ mm/s, values that are typical for the high-spin ($S = 2$) state anticipated for the iron in **1**. Spectra recorded in applied magnetic fields yield an anisotropic magnetic hyperfine tensor with $A_x = +2.3$ (*+1.0*) T, $A_y = A_z = -21.5$ T (*solution*) and a nearly axial zero-field splitting of the spin quintet with $D = D_x \approx -14$ cm^{-1} and rhombicity $E/D \approx 0.1$. The small, positive value for A_x results from the presence of residual orbital angular momentum along *x*. The EPR analysis gives $g_x \approx 2.4$ (and $g_y \approx g_z \approx 2.0$) and reveals a split "$M_S = \pm 2$" ground doublet with a gap distributed around $\Delta = 0.42$ cm^{-1}. The Mössbauer spectra of **1** show unusual features that arise from the presence of orientation-dependent relaxation and a distribution in the magnetic hyperfine field along *x*. The origin of the distribution has been analyzed using crystal field theory. The analysis indicates that the distribution in the magnetic hyperfine field originates from a narrow distribution, $\sigma_\phi \approx 0.5°$, in torsion angle ϕ between the FeN_2 and $FeCl_2$ planes, arising from minute inhomogeneities in the molecular environments.

1. Introduction

Chelating β-diketiminate ligands with bulky 2,6-diisopropylphenyl substituents have become known for their ability to stabilize low-coordinate metal complexes.[1] For example, the reaction of the lithium salt LiL′ with $FeCl_2(THF)_{1.5}$ yields L′FeCl (Figure 1; tert-butyl substituents at the backbone), an iron(II) complex where the coordination number is only three. Interestingly, the coordination number can be tuned by simple ligand modifications. Thus, the analogous reaction with the ligand L (Figure 1; methyl substituents at the backbone) yields the four-coordinate complex $LFeCl_2Li(THF)_2$, complex **1**.[2]

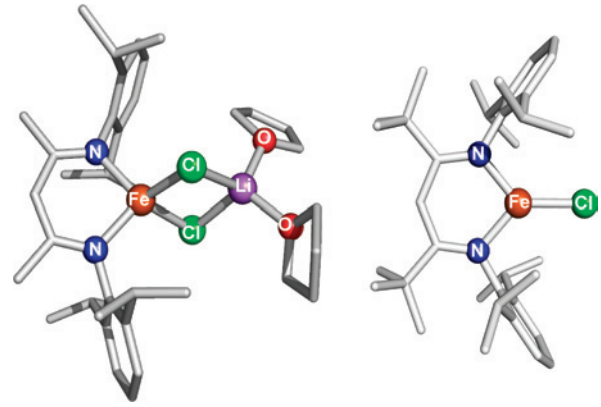

Figure 1. Left: drawing of one of the two molecules in the unit cell from the X-ray structure of $LFe(\mu\text{-}Cl)_2Li(THF)_2$, complex **1.** THF = tetrahydrofuran. Right: drawing of the X-ray structure for L′FeCl.

Andres et al. have investigated the electronic structure of L′FeCl in detail with ^{57}Fe Mössbauer and parallel-mode electron paramagnetic resonance (EPR) spectroscopy, and density functional theory (DFT) calculations.[3] The high-spin

* To whom correspondence should be addressed. E-mail: emunck@cmu.edu (E.M.), eb7g@andrew.cmu.edu (E.L.B.).
† Carnegie Mellon University.
‡ University of Rochester.

(1) Bourget-Merle, L.; Lappert, M. F.; Severn, J. R. *Chem. Rev.* **2002**, *102*, 3031–3066.
(2) Smith, J. M.; Lachicotte, R. J.; Holland, P. L. *Chem. Commun.* **2001**, 1542–1543.

10.1021/ic8004568 CCC: $40.75
Published on Web 09/10/2008

($S = 2$) Fe^{II} site in the three-coordinate complex was shown to have an exceptionally large, axial zero-field splitting (ZFS) and a large, positive internal magnetic field at the iron nucleus. Theoretical analysis indicated that both properties result from spin−orbit coupling between a d_{z^2}-type ground-state and a low-lying d_{yz}-type excited state, with the z axis perpendicular to the diketiminate plane.

In this paper we present the results of spectroscopic and theoretical investigations of the Fe^{II} site in the four-coordinate complex $LFeCl_2Li(THF)_2$. The iron ion in this complex is unambiguously identified as high-spin ($S = 2$) Fe^{II}. The Mössbauer spectra show some remarkable features: the $T <$ 25 K spectra simultaneously exhibit characteristics of (i) both slow and fast relaxation and (ii) the presence of extensive nonrelaxational (heterogeneous) line broadening. Our spectral simulations show that feature (i) can be described by a slightly modified version of a theory for orientation-dependent relaxation proposed by Zimmermann et al.[4] and feature (ii) can be interpreted in terms of a distribution in one of the magnetic hyperfine parameters. The distribution is analyzed using a combination of crystal-field theory (CFT) and DFT calculations. The analysis reveals that the four-coordinate geometry of the iron atom in complex **1** creates conditions under which the Mössbauer spectra are hypersensitive to small distortions of the structure. Quite frequently, spectroscopic studies indicate that some parameters are distributed about their mean values. In EPR work, for instance, one often employs distributions to account for odd line shapes (after checking for relaxation effects), and many researchers use Gaussian distributions in the rhombicity parameter, $\sigma_{E/D}$, of the ZFS and the g-values, σ_g, for spectral simulations. In many cases $\sigma_{E/D}$ is comparable to the range of E/D (one can constrain E/D to the range $0 \leq E/D \leq 1/3$), which suggests qualitatively that the compound is structurally very heterogeneous. Unfortunately, it is generally difficult to quantitatively correlate the σ values with bond lengths and bond angles, in particular for high-spin iron(III) complexes. The present study offered the opportunity to identify the sources of the spectroscopic heterogeneities, and interestingly the heterogeneous broadening was found to be correlated with a distribution of the torsion angle between the FeN_2 and $FeCl_2$ planes that is so small ($\sigma = 0.5°$) to be imperceptible even in a high resolution X-ray structure.

2. Materials and Methods

Complex **1** was synthesized and purified using standard air-free techniques, according to the literature.[2,5] Mössbauer samples were transported in specially designed Delrin cells with tight-fitting caps (shrink fits), which were kept at 77 K during transport inside capped test tubes. Benzene solutions for EPR spectroscopy were kept in flame-sealed quartz tubes.

Mössbauer spectra were recorded on two spectrometers, using Janis Research Super-Varitemp Dewar flasks that allowed studies in applied magnetic fields up to 8.0 T in the temperature range from 1.5 to 140 K. Initial simulations of the Mössbauer data were performed using the WMOSS software package (WEB Research, Edina, MN). Further refinement of our analysis was performed with a modified version of the Mössbauer spectra simulation program SP*in*H*amiltonian*MOSS*bauer* (SPHMOSS) developed by Münck et al.,[6] to allow for the change in relaxation during powder integration and distribution of hyperfine fields as described in the text. Isomer shifts are quoted relative to Fe metal at 298 K.

EPR spectra were recorded on a Bruker EPR 300 spectrometer equipped with an Oxford ESR 910 liquid helium cryostat and an Oxford temperature controller. EPR spectra were simulated using the program SpinCount written by Dr. M. P. Hendrich at Carnegie Mellon University.[7]

DFT calculations were performed using Gaussian '03 (revision D.01) software package,[8] using the hybrid functional B3LYP[9,10] and the triple-ζ basis set 6−311G. Self-consistent field (SCF) and geometry calculations were performed with default convergence criteria. The ground-state character of the SCF solution was corroborated by time-dependent density-functional theory (TD-DFT) calculations, which yielded exclusively positive excitation energies. The crystal field (CF) analysis was performed using a locally developed Fortran code (see Supporting Information).

3. Results

We have studied Mössbauer spectra of **1** in polycrystalline form and frozen benzene solution between 1.5 and 140 K in magnetic fields up to 7.0 T applied parallel to the γ beam. Representative spectra are shown in Figures 2−4. The data were analyzed in the framework of the $S = 2$ spin Hamiltonian

$$\hat{H} = D\left\{\hat{S}_x^2 - \frac{1}{3}S(S+1) + \frac{E}{D}\left(\hat{S}_y^2 - \hat{S}_z^2\right)\right\} + \beta\mathbf{B}\cdot\mathbf{g}\cdot\hat{\mathbf{S}} + \hat{\mathbf{S}}\cdot\mathbf{A}\cdot\hat{\mathbf{I}} - \beta_n g_n \mathbf{B}\cdot\hat{\mathbf{I}} + \hat{H}_Q \quad (1a)$$

with

$$\hat{H}_Q = \frac{1}{12}eQV_{xx}\left[3\hat{I}_x^2 - I(I+1) + \eta\left(\hat{I}_y^2 - \hat{I}_z^2\right)\right] \quad (1b)$$

In eq 1a we have chosen the x-axis rather than the conventional z-axis as the direction associated with the ZFS

(3) Andres, H.; Bominaar, E. L.; Smith, J. M.; Eckert, N. A.; Holland, P. L.; Münck, E. *J. Am. Chem. Soc.* **2002**, *124*, 3012–3025.
(4) Zimmerman, R.; Spiering, H.; Ritter, G. *Chem. Phys.* **1974**, *4*, 133–141.
(5) Holland, P. L.; Cundari, T. R.; Perez, L. L.; Eckert, N. A.; Lachicotte, R. J. *J. Am. Chem. Soc.* **2002**, *124*, 14416–14424.
(6) Münck, E.; Groves, J. L.; Tumolillo, T. A.; Debrunner, P. G. *Comput. Phys. Commun.* **1973**, *5*, 225–238.
(7) The simulation software used in this paper for analyzing EPR spectra can be downloaded from http://www.chem.cmu.edu/groups/hendrich/facilities/index.html.
(8) Frisch, M. J.; Trucks, G. W.; Schlegel, H. B.; Scuseria, G. E.; Robb, M. A.; Cheeseman, J. R.; Montgomery, Jr., J. A.; Vreven, T.; Kudin, K. N.; Burant, J. C.; Millam, J. M.; Iyengar, S. S.; Tomasi, J.; Barone, V.; Mennucci, B.; Cossi, M.; Scalmani, G.; Rega, N.; Petersson, G. A.; Nakatsuji, H.; Hada, M.; Ehara, M.; Toyota, K.; Fukuda, R.; Hasegawa, J.; Ishida, M.; Nakajima, T.; Honda, Y.; Kitao, O.; Nakai, H.; Klene, M.; Li, X.; Knox, J. E.; Hratchian, H. P.; Cross, J. B.; Bakken, V.; Adamo, C.; Jaramillo, J.; Gomperts, R.; Stratmann, R. E.; Yazyev, O.; Austin, A. J.; Cammi, R.; Pomelli, C.; Ochterski, J. W.; Ayala, P. Y.; Morokuma, K.; Voth, G. A.; Salvador, P.; Dannenberg, J. J.; Zakrzewski, V. G.; Dapprich, S.; Daniels, A. D.; Strain, M. C.; Farkas, O.; Malick, D. K.; Rabuck, A. D.; Raghavachari, K.; Foresman, J. B.; Ortiz, J. V.; Cui, Q.; Baboul, A. G.; Clifford, S.; Cioslowski, J.; Stefanov, B. B.; Liu, G.; Liashenko, A.; Piskorz, P.; Komaromi, I.; Martin, R. L.; Fox, D. J.; Keith, T.; Al-Laham, M. A.; Peng, C. Y.; Nanayakkara, A.; Challacombe, M.; Gill, P. M. W.; Johnson, B.; Chen, W.; Wong, M. W.; Gonzalez, C.; and Pople, J. A. *Gaussian 03*, Revision D.01; Gaussian, Inc.: Wallingford CT, 2004.
(9) Becke, A. D. *J. Chem. Phys.* **1993**, *98*, 5648–5652.
(10) Lee, C.; Yang, W.; Parr, R. G. *Phys. Rev. B* **1988**, *37*, 785–789.

Table 1. Hyperfine Parameters of **1** in Solid and Frozen Solution Samples[a]

		EFG		*A*-tensor				ZFS		*g*-tensor		
sample	δ [mm/s]	ΔE_Q [mm/s]	η	A_x^0 [T]	σ_A [T]	A_y [T]	A_z [T]	D [cm^{-1}]	E/D	g_x	g_y	g_z
solid	0.90(2)	2.40(2)	0.75(2)	2.3(1)	1.0(2)	−21.5(4)	−21.5(4)	−14(2)	0.10(4)	2.4(2)	2.0	2.0
solution	0.90(2)	2.40(2)	0.75(2)	1.0(1)	2.0(2)	−21.5(4)	−21.5(4)	−14(2)	0.10(4)	2.4(2)	2.0	2.0

[a] Numbers in parentheses are estimated uncertainties for the last digits.

parameter D. This choice connects the spin Hamiltonian analysis with our previous DFT and CF calculations of iron β-diketiminate complexes.[3,11] The Hamiltonian in eq 1a is most conveniently diagonalized when the electronic spin is quantized along x, that is, $\hat{S}_x|S,M_s\rangle = M_s|S,M_s\rangle$. The same axes were used in the definition of the nuclear quadrupole coupling operator, eq 1b. Theoretical calculations presented below show that x is in the plane of the β-diketiminate ligand, bisecting the N−Fe−N angle.

The solid lines drawn through the spectra of Figures 2−4 are spectral simulations based on eqs 1a,b using the parameters listed in Table 1. In anticipation of the following analysis, we notice that orientation-dependent spin−lattice relaxation, as well as distributions in the values for the x component of the magnetic hyperfine tensor, A_x, are affecting the spectra profoundly. While these effects are felt for most spectra of our data set of 30 Mössbauer spectra, we will illustrate them briefly for the 1.0 T spectra recorded at 4.2 K (Figure 4).

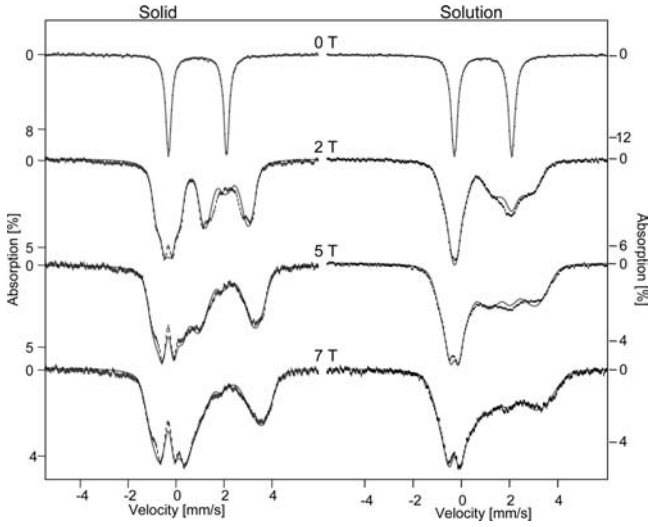

Figure 2. Mössbauer spectra at 4.2 K recorded in applied magnetic fields as indicated for complex **1** as a solid (left) and in frozen benzene solution (right). The solid lines are simulations that account for both the change in relaxation regime using $\Delta_{relax} = 1.4(2)$ cm^{-1} (see text) as well as for the distribution in the magnetic hyperfine field along x, using the parameters presented in Table 1.

Complex **1** has a negative ZFS parameter, $D = -14(2)$ cm^{-1}, and the ZFS tensor is (roughly) axial, $E/D = 0.10$. Consequently, the electronic ground state is the "$M_S = \pm 2$" quasi doublet of the $S = 2$ manifold. (N.B. Because E/D is finite, M_S is not strictly a good quantum number and the doublet is split in two singlet states of the form $|\varphi_\pm\rangle \approx 2^{-1/2}(|M_S = +2\rangle \pm |M_S = -2\rangle)$ that are separated by energy $\Delta = 3D(E/D)^2 = 0.42$ cm^{-1}.) The properties of this doublet determine the essential features of the 4.2 K spectra. Because the $\varphi_\pm$ levels are nonmagnetic, the Mössbauer spectra exhibit a quadrupole doublet in the absence of an applied magnetic field. At 4.2 K complex **1** has $\Delta E_Q = 2.40(2)$ mm/s and isomer shift $\delta = 0.90(2)$ mm/s, strongly suggesting the presence of a high-spin ($S = 2$) Fe^{II} site[12] as expected for the coordination environment. The 7.0 T spectra recorded for solid **1** at 140 K (Figure 3 bottom, left) and in solution at 100 K (bottom, right) show that $\Delta E_Q > 0$ and the asymmetry parameter $\eta = |V_{yy} - V_{zz}|/V_{xx}$ of the electric field gradient tensor is about 0.75. The applied field, B, mixes the two levels of the ground doublet, inducing magnetic hyperfine interactions as shown in Figures 2 and 3. The particular values of D and E/D render each of the two lowest spin levels magnetically uniaxial, with the easy axis of magnetization along x.

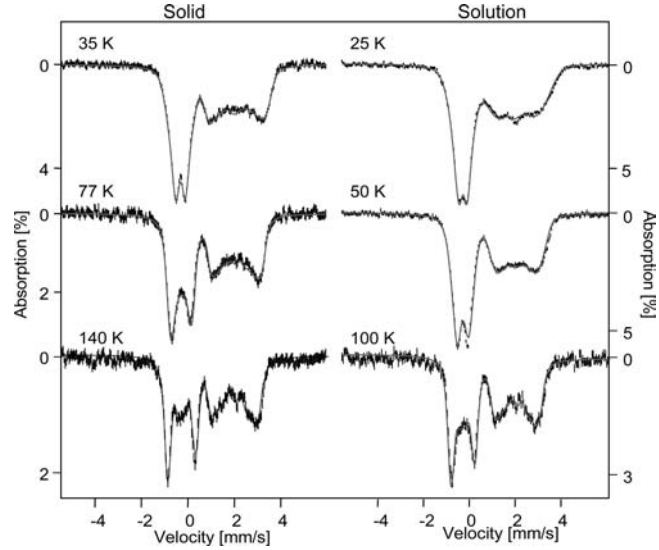

Figure 3. Variable temperature Mössbauer spectra recorded in an applied field of 7.0 T for solid **1** (left) and in frozen benzene solution (right). The solid lines represent simulations obtained in the fast relaxation regime, taking in account the distribution in hyperfine field along x, using the parameters of Table 1.

The 1.0 T spectrum of **1** (Figure 4) has a low-energy peak with distinct shoulders on each side, indicated by arrows in the solid state spectrum where these features are most prominent. The presence of shoulders suggests orientation-dependent spin−lattice relaxation as shown more than 30 years ago by Zimmermann in a Mössbauer study of $[FeL_4](ClO_4)_2$, where L = 1,8-naphthydrine.[4] The spectral

(11) (a) Stoian, S. A.; Yu, Y.; Smith, J. M.; Holland, P. L.; Bominaar, E. L.; Münck, E. *Inorg. Chem.* **2005**, *44*, 4915–4922. (b) Stoian, S. A.; Vela, J.; Smith, J. M.; Sadique, A. R.; Holland, P. L.; Münck, E.; Bominaar, E. L. *J. Am. Chem. Soc.* **2006**, *128*, 10181–10192. (c) Eckert, N. A.; Stoian, S.; Smith, J. M.; Bominaar, E. L.; Münck, E.; Holland, P. L. *J. Am. Chem. Soc.* **2005**, *127*, 9344–9345.

(12) Gütlich, P.; Link, R.; Trautwein, A. *Mössbauer Spectroscopy and Transition Metal Chemistry*; Springer-Verlag: Berlin, Germany, 1978.

simulations of Figure 4 (bottom; solid line) were generated by assuming that the samples contain two molecular populations, one relaxing fast in comparison with the Mössbauer time scale (ca. 10^{-7} s) and the other slow. Because the relaxational phenomena persist in the dilute solution sample (Figure 4, right), the underlying interaction is spin−lattice rather than spin−spin in nature. Our observations can be understood by considering the magnetic properties of the ground quasi doublet. Owing to the particular values of D and E/D, the doublet has a large Zeeman splitting for B applied along x (effective g-value $g_{\text{eff}} \approx 9.9$), whereas the Zeeman splitting is small when the field is directed along the molecular yz plane. Our simulations assume fast relaxation for orientations of the molecule relative to the applied magnetic field for which the ground doublet has a combined zero-field and Zeeman splitting of less than $\Delta_{\text{relax}} = 1.4(2)$ cm^{-1},[13] and slow relaxation for orientations that generate larger splittings. For a given field strength, the surface of the field orientation sphere is partitioned in two areas, one pertaining to slow relaxation and the other to fast relaxation. The slow relaxation area consists of two patches that are centered at the poles of the orientational sphere where the largest magnetic field component is along the easy magnetization axis, x. The area with fast relaxation is located in the equatorial zone, where the largest field component is along the yz plane. The polar caps grow upon increasing the magnetic field at the expense of the equatorial zone, which leads to a reduction of the fast relaxation peak at the center of the right line (Figure 2, right). There must be, of course, a transition region between the fast and slow relaxation regimes, but our data are not sensitive enough to reveal intermediate relaxation. At temperatures above 20 K fast relaxation is observed for all molecular orientations.

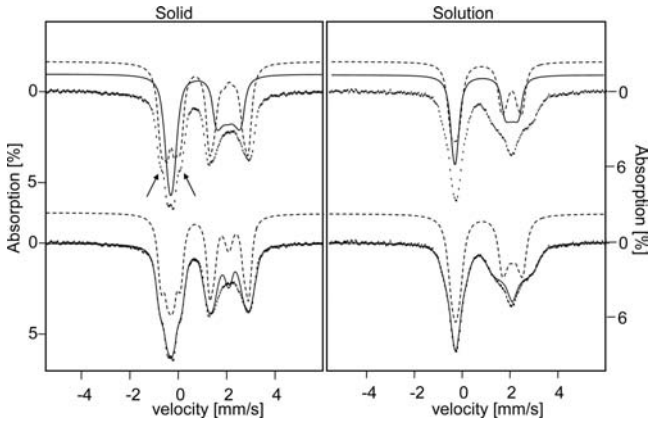

Figure 4. Spectra at 1.0 T recorded at 4.2 K for complex **1** in solid (left) and in frozen benzene solution (right). Top: the solid lines represent simulations obtained for fast relaxation while dashed lines are obtained for slow relaxation (see text). Bottom: dashed lines represent simulations taking in account orientation-dependent relaxation, using $\Delta_{\text{relax}} = 0.75(5)$ cm^{-1}; the solid lines represent the simulations obtained in the presence of both orientation-dependent relaxation and a distribution in A_x (see text).

Let us now take a closer look at the spectra of Figure 4. The solid and dashed lines (top) are simulations assuming fast and slow relaxation, respectively, and both provide poor fits of the data. The simulations using the orientation-dependent relaxation model (dashed line, bottom) reproduce, as anticipated, the shoulders of the low-energy peak but fail to account for the width of the high-energy feature. The splitting of this feature depends critically on the x-component of the magnetic hyperfine tensor, and in order to properly simulate this feature we assumed that A_x has a Gaussian distribution of width σ_A around its mean value, A_x^0. Although A_x is by far the smallest component of the magnetic hyperfine tensor (Table 1), it is sensitively felt in the low-field spectra because it acts along the easy magnetization axis of the electronic system. The distribution broadens the peaks of the slow relaxation spectrum that underlies the shoulders of both the low-energy feature and the two exterior peaks of the high-energy feature of the spectra in Figures 2 and 4 but hardly affects the quadrupole doublet-like spectral component that pertains to the fast relaxing species (solid line, Figure 4, top) since the hyperfine field therein practically vanishes. Additional contributions to the intensity of the doublet component arise from slow relaxing species for which the distribution gives $A_x \approx 0$.[14] Altogether, these transformations give the high-energy feature of the solution spectrum the characteristic shape of a spiked Prussian helmet (Figure 4, bottom, right). Note that A_x is the only parameter that differs noticeably between the solid and frozen solution; see Table 1. For the solid (*solution*) sample we found different values for $A_x/g_n\beta_n = +2.3$ *(+1.1)* T with $\sigma_A \approx +1$ *(+2)* T. We show below that the distribution of A_x reflects a distribution, $\sigma_\phi = 0.56°$ *(1.06°)*, of the dihedral angle ϕ between the ClFeCl plane and the diketiminate plane.

The spectral simulations displayed in Figures 2 and 3 are compromises that best fit a representative set of 12 spectra each, using the same set of parameter values. Not surprisingly, one can find better fits to individual spectra, except for the 2 T spectra of the solid. The 2 T spectrum of the solid exhibits fine structure around 1 and 3 mm/s Doppler velocity that we cannot attribute to relaxation and distribution effects. We attribute this phenomenon to multiple crystal forms of **1**. As reported in ref 2 there are two different ways that **1** can pack (space groups $Pna2_1$ and $P2_12_12_1$). In the first crystal form, there are two crystallographically distinct iron environments, and in the latter, there are three crystallographically distinct iron environments. In the various structures, the Fe−N distances vary from 1.998(3) to 2.021(4) Å, the Fe−Cl distances vary from 2.319(1) to 2.338(1) Å, and the N−Fe−Cl angles vary from 111.8(1) to 124.6(1) degrees. Variations in the molecular micro environments in the frozen solution presumably lead to a broader range of metrical parameters, increasing the heterogeneity.

In zero magnetic field the "$M_S = \pm 2$" ground doublet is split by $\Delta = 0.42$ cm^{-1}, which is larger than the microwave quantum at X-band. However, it is well-known from integer

(13) This value was used for simulations of spectra with $B > 1.5$ T; the spectra recorded in 0.5 and 1.0 T required a somewhat smaller value, $\Delta_{\text{relax}} \approx 0.75(5)$ cm^{-1}.

(14) Since A_x^0 has a small value, the distribution has significant amplitude at $A_x \approx 0$.

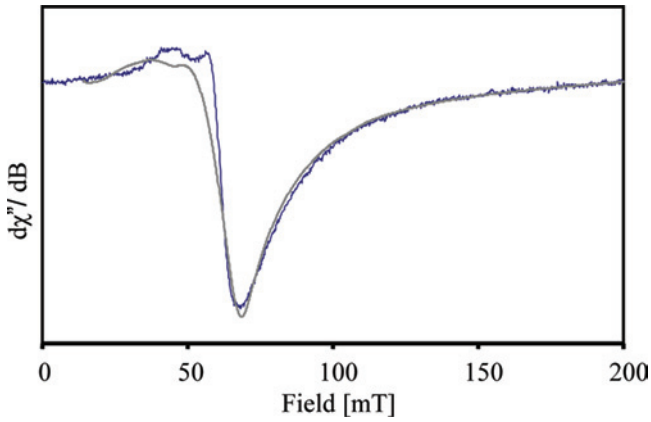

Figure 5. X-band EPR derivative spectrum recorded in parallel mode at 6.5 K for a frozen benzene solution of complex **1**. The solid line represents a simulation using $D = -14.0$ cm^{-1}; $E/D = 0.072$; $\sigma_{E/D} = 0.014$; $g_x = 2.4$; $g_z = g_y = 2.0$; ($\sigma_{gx} = \sigma_{gy} = \sigma_{gz} = 0$) with a packet Lorentzian line width of 1.8 mT. The minimum of the derivative spectrum is at $g_{eff} \approx 9.9$.

spin EPR work[15] that D and E/D are often distributed such that a substantial fraction of molecules in the sample has Δ-values smaller than $h\nu \approx 0.3$ cm^{-1}, allowing integer-spin EPR signals to be observed at X-band. Figure 5 shows an EPR spectrum of **1** recorded in benzene solution in parallel mode at 6.5 K. For a magnetic field along x, the resonance condition for **1** is given by

$$h\nu = \sqrt{\Delta^2 + (4g_x\beta B_x)^2} \qquad (2)$$

The unknowns in eq 2 are the splitting of the quasi doublet in zero field, Δ, and g_x. Determination of Δ and g_x from EPR alone would require measurements at multiple frequencies. We used instead the Mössbauer result for Δ, deduced from the values of D and E/D, and varied g_x (σ_{gx} has a minor influence on the simulations and was set equal to zero) and $\sigma_{E/D}$ to obtain, for $g_x = 2.4$, the theoretical curve of Figure 5.

4. Discussion

4.1. Crystal-Field Model. In order to rationalize the spectroscopic data for **1**, we have analyzed the energies and compositions of the iron 3d orbitals of this complex with a CF model in which point charges carrying charge q were placed at the positions of the iron-bound atoms (Figure 6). For comparison, a similar analysis was performed for the complex LFe^{II}Cl (L = β-diketiminate) that was characterized in an earlier study.[3] The Fe−Cl and Fe−N(diketiminate) distances were fixed to those obtained from the DFT geometry optimized structure for the model shown in Figure 6 with imposed C_{2v} point group symmetry. As the diketiminate ligand is a rigid system, the N−Fe−N angle was kept constant in the CF analysis. Potential energy surfaces obtained with DFT calculations show that torsion angle ϕ and bond angle θ defined in Figure 6 are the "softest" structural parameters in the coordination sphere of iron. Soft coordinates have small elastic force constants and are therefore susceptible to distortion by external forces, which suggests that distributions in the values for ϕ and θ are the structural source for the distribution in the hyperfine coupling constant A_x.

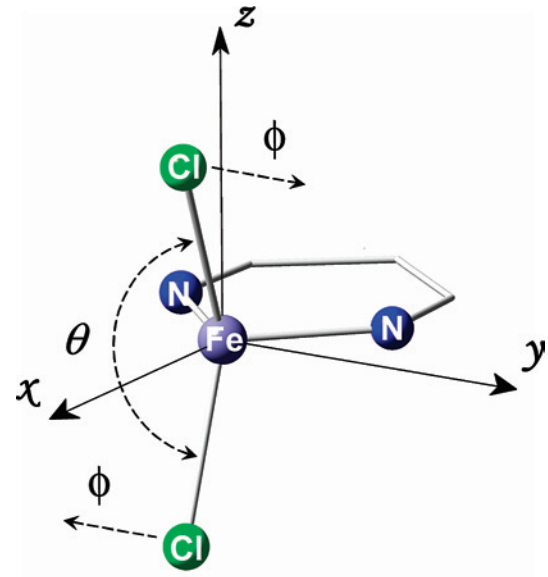

Figure 6. Two angles considered in the analysis of the distribution function for A_x. θ is the Cl−Fe−Cl bite angle and ϕ rotates the ClFeCl plane around the bisector of the N−Fe−N angle (x axis) relative to the β-diketiminate plane. $\phi = 0°$ corresponds to the orthogonal conformation. The easy axis of magnetization is along x.

The CF calculations of the three-coordinate complex LFe^{II}Cl yield a d_{z^2} ground state and d_{yz} as the first excited state at a few hundred wavenumbers above the ground state, where the z axis is defined perpendicular to the diketiminate plane (Figure 6). In the CF calculation for the four-coordinate complex **1**, the d_{z^2} and d_{yz} levels are interchanged, $\Delta_1 = \varepsilon(d_{z^2}) - \varepsilon(d_{yz}) > 0$. The other 3d levels occur at $\varepsilon(d_{xz}) < \varepsilon(d_{x^2-y^2}) < \varepsilon(d_{xy})$ and are at least 4000 cm^{-1} above the d_{z^2} and d_{yz} levels. The symmetry of the CF for torsion angle $\phi = 0°$ (Figure 6) is C_{2v} and forbids d_{yz} (b_1) and d_{z^2} (a_1) to mix. For $\phi \neq 0°$ the symmetry is lowered to C_2 such that the d_{yz} (a) and d_{z^2} (a) interact under the influence of the CF. The resulting 3d orbitals,

$$\psi_g = \cos(\omega)d_{yz} + \sin(\omega)d_{z^2} \qquad (3a)$$

$$\psi_e = -\sin(\omega)d_{yz} + \cos(\omega)d_{z^2} \qquad (3b)$$

are characterized by the mixing parameter $\omega = \omega(\phi)$, which is a function of torsion angle ϕ. The admixture of the lowest two orbitals with the much higher lying $d_{x^2-y^2}$ (a) is small and has been ignored. The magnetic sublevels of the high-spin d^6 configurations, $|\psi_g M_S\rangle$ and $|\psi_e M_S\rangle$, in which the sixth d electron is respectively occupying the orbitals ψ_g and ψ_e, are labeled with the magnetic spin quantum number $M_S = \pm 2, \pm 1$, and 0, where the 2-fold symmetry axis, x, has been taken as the spin quantization axis, that is, $\hat{S}_x|M_S\rangle = M_S|M_S\rangle$, for reasons presented in the next section.

4.2. Spin−Orbit Coupling. The lowest two d^6 configurations interact via spin−orbit coupling, $\lambda\hat{\mathbf{L}}\cdot\hat{\mathbf{S}}$. The one-electron orbital momentum operator $\hat{\mathbf{l}}$ has only one non-zero

(15) (a) Hendrich, M. P.; Debrunner, P. G. *Biophys. J.* **1989**, *56*, 489–506. (b) Surerus, K. K.; Hendrich, M. P.; Christie, P. D.; Rottgardt, D.; Orme-Johnson, W. J.; Münck, E. *J. Am. Chem. Soc.* **1992**, *114*, 8579–8590. (c) Münck, E.; Surerus, K. K.; Hendrich, M. P. *Methods Enzymol.* **1993**, *227*, 463–479.

matrix element in the basis $\{\psi_g, \psi_e\}$, $\langle\psi_e|\hat{l}_x|\psi_g\rangle = i\sqrt{3}$, which is independent of ω. As a consequence, the spin−orbit coupling operator is equivalent to the operator $\lambda\,\hat{L}_x\hat{S}_x$ in the space spanned by the states $|\psi_{g,e}M_S\rangle$. A perturbation treatment of the spin−orbit coupling results in the states

$$|\psi_{M_S}M_S\rangle \approx \left|\left(\psi_g - \frac{i\sqrt{3}\lambda M_S}{\Delta_1}\psi_e\right)M_S\right\rangle \quad (4)$$

Δ_1 denotes the CF splitting between ψ_e and ψ_g and is a function of the angle ϕ. The orbital angular moment of these states is partially unquenched along x,

$$\langle\psi_{M_S}M_S|\hat{L}_x|\,\psi_{M_S}M_S\rangle \approx -\frac{6M_S\lambda}{\Delta_1} \quad (5)$$

and vanishes along y and z. The relative energies of the M_S states are described by the spin operator $D_x\hat{S}_x^2$ with a negative ZFS parameter, $D_x < 0$. The ZFS is axial, $D = D_x$, when spin−orbit mixing with states other than those of eqs 3a,b is ignored. The lowest two magnetic sublevels form a degenerate doublet, $M_S = \pm 2$, that is split in a magnetic field, yielding an $M_S = -2$ ground-state with orbital angular moment

$$\langle L_x\rangle = \langle\psi_{-2}, -2|\hat{L}_x|\,\psi_{-2}, -2\rangle \approx 12\left(\frac{\lambda}{\Delta_1}\right) \quad (6)$$

This quantity determines the g-value along x (g_x), the ZFS parameter (D), and the orbital term of the magnetic hyperfine tensor ($A_{L,x}$):

$$\Delta g_x = g_x - 2 \approx -{}^1\!/_2\langle L_x\rangle \approx -6\left(\frac{\lambda}{\Delta_1}\right) \quad (7a)$$

$$D = D_x \approx -{}^1\!/_4\lambda\langle L_x\rangle \approx -3\lambda\left(\frac{\lambda}{\Delta_1}\right) \quad (7b)$$

$$A_{L,x} \approx -{}^1\!/_2P\langle L_x\rangle \approx -6P\left(\frac{\lambda}{\Delta_1}\right) \quad (7c)$$

We note that it is the mixing of the same orbitals, d_{yz} and d_{z^2}, that determines the magnetic properties of the four-coordinate $LFeCl_2Li(THF)_2$, **1**, and the three-coordinate L′FeCl of ref 3. However, in the latter case the two CF levels are nearly degenerate, and spin−orbit coupling acts in first-order, leading to a large unquenched orbital angular momentum.

4.3. Calibration of CF Model. In the following analysis we have adopted a frequently used value for the spin−orbit coupling constant λ of -80 cm^{-1}, which is 20% smaller in magnitude than the free-ion value $\lambda^o \approx -100$ cm^{-1} to account for covalency. The fundamental scaling factor of the magnetic hyperfine interaction, $P = g_e g_n \beta\beta_n\langle r^{-3}\rangle_{3d}$, is conventionally expressed in magnetic field units by taking the ratio $P/g_n\beta_n$. Its value is found to be 64 T for free Fe^{II}, based on numerical Hartree−Fock solutions for the radial 3d functions.[16] Adopting a similar covalent reduction as for λ we obtain $P/g_n\beta_n \approx 50$ T for Fe^{II} in the present coordination environment. The magnetic hyperfine constant is composed of three contributions, namely, the Fermi contact term, the orbital term, and the spin-dipolar term: $A_x = A_{FC,x} + A_{L,x} + A_{SD,x}$. The Fermi contact term for free Fe^{II} is $A_{FC}^0 \approx -27.5$ T and yields, after a ∼20% covalent reduction, $A_{FC} \approx -22.5$ T. $A_{SD,x} \approx P/7$ for the d^6 configuration in which the d_{yz} orbital is doubly occupied. Its value is slightly reduced (by ∼10%) due to d_{z^2} admixture (eqs 3a,b) and has the value $A_{SD} \approx +6.4$ T. Given that, apart from Δ_1, all parameters have now been assigned values, the expressions in eqs 7a−7c, in order to be applicable, must reproduce the experimental values $\Delta g_x = 0.4(0.2)$, $D_x = -14(2)$ cm^{-1}, and $A_x = +2.3$ T/*+1.1* T (solid/*solution)* for a single value for Δ_1. It appears that this is indeed the case. Thus, for $\Delta_1 = 1370$ cm^{-1} we obtain the values $\Delta g_x = 0.35$ and $D_x = -14$ cm^{-1}, which are both within the experimental error margins, and $A_{L,x} = +17.5$ T, which combined with the values for A_{FC} and A_{SD} gives a total of $A_x = +1.4$ T that is in the range for this quantity defined by the solid state and solution samples. The ratio $\lambda/\Delta_1 \approx -0.058$ for $\lambda = -80$ cm^{-1} and $\Delta_1 = 1370$ cm^{-1} yields $\langle L_x\rangle \approx -0.7$. This value is reached at the experimental value $\phi \approx 10°$ (Figure 7), which is achieved by properly adjusting the effective charge of the CF model that acts as an overall scaling factor of the 3d level scheme. After the CF model has thus been calibrated to match the data for **1**,

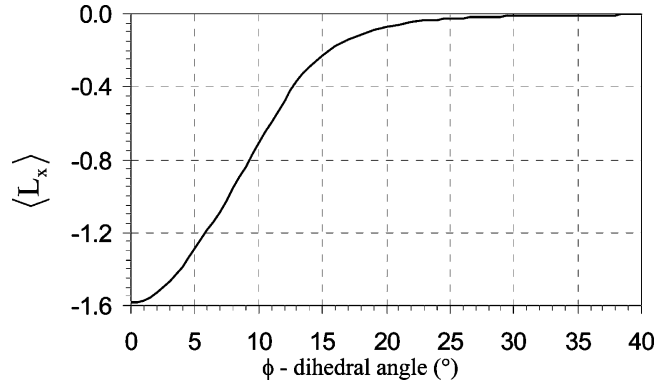

Figure 7. Orbital angular moment along x vs ϕ in a magnetic field of 0.1 T applied along x obtained by a full CF calculation.

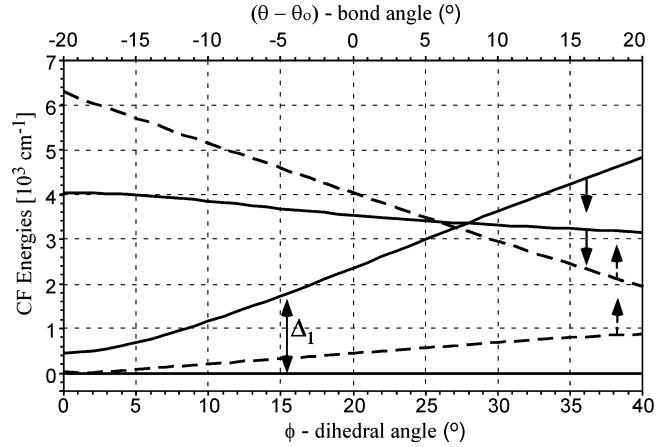

Figure 8. Energies of the lowest two CF excited states vs ϕ for $\theta = \theta_0$ fixed (solid lines, bottom abscissa, see arrows) and vs $(\theta - \theta_0)$ for $\phi = 0°$ fixed (dashed lines, top abscissa, see arrows); $\theta_0 = 110.2°$. The ground-state energy has been taken as the origin of the energy scale for all values of ϕ and θ. The structure has C_{2v} point group symmetry for $\phi = 0°$ and C_2 symmetry otherwise.

(16) Abragam, A.; Bleaney, B. *Electron Paramagnetic Resonance of Transition Ions;* Clarendon Press: Oxford, 1970; Chapter 17.

we can address the structural origin of the distribution in the magnetic hyperfine field.

4.4. Origin of Distribution in A_x. The Mössbauer analysis of complex **1** revealed that the magnetic hyperfine field along the molecular magnetization axis (x) can be modeled as a Gaussian type distribution,

$$P_A(A_x) = N_A \exp[-(A_x - A_x^0)^2/2\sigma_A^2] \quad (8)$$

The distribution has a maximum at A_x^0 and a standard deviation σ_A. As a consequence, all quantities that are linearly related to small variations in A_x, notably $\langle L_x \rangle$, ϕ, and Δ_1, should also exhibit Gaussian distributions. The maxima and standard deviations of these distributions are denoted $\langle L_x \rangle^0$ and σ_L for $\langle L_x \rangle$, ϕ^0 and σ_ϕ for ϕ, and Δ^0 and σ_Δ for Δ_1. The standard deviations are related by the expressions

$$\sigma_L = 2\sigma_A/P \quad (9a)$$

$$\sigma_\phi = \sigma_L \left(\frac{d\langle L_x \rangle}{d\phi} \right)^{-1}_{\phi^0} \quad (9b)$$

$$\sigma_\Delta = \sigma_\phi \left(\frac{d\Delta_1}{d\phi} \right)_{\phi^0} \quad (9c)$$

$$\sigma_f = 2K\sigma_\phi \quad (9d)$$

Equation 9a follows from eq 7c, the factor in eq 9b is the reciprocal tangent of the slope of $\langle L_x \rangle$ versus ϕ at $\phi^0 \approx 10°$ in Figure 7, the derivative in eq 9c is the tangent of the first excitation energy Δ_1 versus ϕ plot at ϕ^0 in Figure 8, and eq 9d will be discussed below. Using the experimental standard deviations $\sigma_A = 1.0/\textit{1.9}$ T, $P = 50$ T, and the numerical values for the derivatives, we obtain for the standard deviations the values $\sigma_L = 0.040/\textit{0.076}$, $\sigma_\phi = 0.36°/\textit{0.68}°$, and $\sigma_\Delta = 63$ cm^{-1}/*119* cm^{-1} (solid/*solution*).

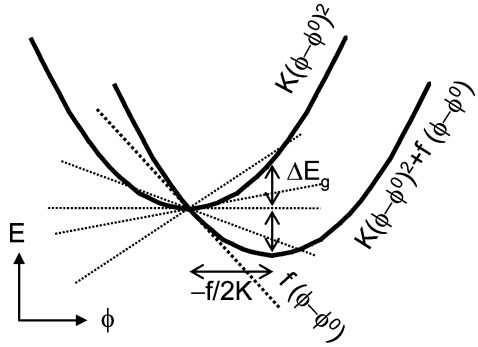

Figure 9. Influence of random potential on equilibrium conformation and energy. A Gaussian distribution in f gives a Gaussian distribution in the displacement $-f/(2K)$ and non-Gaussian distribution in the energy difference ΔE_g (cf. eq 13).

The distributions can be explained by assuming that the molecules are exposed to a small, "random" potential, $F(\phi) \ll \Delta_1$, arising from slight differences in the surroundings of the complexes. The potential for a given molecule can be expanded as $F(\phi) \approx f' + f(\phi - \phi^0)$. Since $F \sim f' \ll \Delta_1$, the constant term has only a minor influence on the excitation energy and is therefore neglected.[17] The ϕ dependence near the equilibrium angle ϕ^0 of the ground-state energy of the complex in vacuum can be approximated as $K(\phi - \phi^0)^2$, where K is a force constant. By adding the two potentials we obtain the expression for the ϕ dependence of the ground-state energy of the molecule in the medium,

$$E_g \approx K(\phi - \phi^0)^2 + f(\phi - \phi^0) \quad (10)$$

The two potentials and their sum are illustrated in Figure 9. The linear term of the random potential displaces the potential minimum by

$$\Delta\phi = -\frac{f}{2K} \quad (11)$$

The linear relationship between $\Delta\phi$ and f implies that if parameter f is distributed around $f^0 = 0$ according to a Gaussian distribution, then ϕ, $\langle L_x \rangle$, and Δ_1 must be Gaussian distributed as well.[18] Equation 11 implies that the standard deviations of f and ϕ are related as $\sigma_f = 2K\sigma_\phi$ (eq 9d). We have estimated K from DFT calculations to be 0.78 cm^{-1}/(deg)^2 (see below). Using this estimate we obtain $\sigma_f = 0.56$ cm^{-1}/deg/*1.06* cm^{-1}/deg (solid/*solution*). The random potential lowers the ground-state energy by

$$\Delta E_g = \frac{f^2}{4K} = K(\Delta\phi)^2 \quad (12)$$

The quadratic dependence of ΔE_g on f translates into a non-Gaussian distribution for the ground-state energy,

$$P_E(\Delta E_g) = N_\phi (K\Delta E_g)^{-1/2} \exp[-(\Delta E_g)^2/2K\sigma_\phi^2] \quad (13)$$

The distribution function in eq 13 is defined for positive values of ΔE_g and approaches infinity in the zero-energy limit but can nonetheless be normalized.

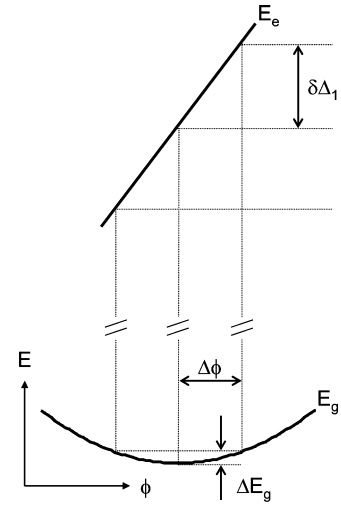

Figure 10. Relation between variations ΔE_g (bottom arrows), $\Delta\phi$ (middle arrow), and $\delta\Delta_1$ (top arrow).

The change in the ground-state energy for distortion $\Delta\phi = \sigma_\phi$ is $\Delta E_g = 0.10$ cm^{-1}/*0.36* cm^{-1} (solid/*solution*) and is a measure of the energy required for inducing the distribution in Δ_1 ($\delta\Delta_1 \sim 100$ cm^{-1}) and related quantities. To understand how a change in the ground-state energy as small as ~0.2

(17) The quadratic term of the random potential is much smaller than the harmonic potential of the molecule and has therefore been neglected as well.

(18) The conservation of distribution function type is generally valid and not specific for Gaussian distributions.

cm^{-1} can induce a 3 orders of magnitude larger change in excitation energy Δ_1 ($\delta\Delta_1 \sim 100\ cm^{-1}$) we consider the derivative $d\Delta_1/d\Delta E_g$. Using the expression

$$\left(\frac{d\Delta E_g}{d\phi}\right)_{\phi^0} = \sqrt{4K\Delta E_g} \tag{14a}$$

we obtain

$$\frac{d\Delta_1}{d\Delta E_g} = \left(\frac{d\Delta_1}{d\phi}\right)_{\phi^0}\left(\frac{d\Delta E_g}{d\phi}\right)^{-1}_{\phi^0} = \frac{1}{\sqrt{4K\Delta E_g}}\left(\frac{d\Delta_1}{d\phi}\right)_{\phi^0} \tag{14b}$$

The derivative in eq 14b approaches infinity for $\Delta E_g \rightarrow 0$, given that $(d\Delta_1/d\phi)_{\phi^0}$ is a nonzero quantity.[19] The relation between the variations $\delta\Delta_1$ and $\delta\Delta E_g$ is illustrated in Figure 10. The linear term of the random potential f ($\sim 1\ cm^{-1}$/deg) is much smaller than $(d\Delta_1/d\phi)_{\phi^0} \approx 175\ cm^{-1}$/deg and has therefore a negligible influence on the rate of change of the excitation energy.

The analysis presented here is generally applicable and shows that distortions associated with minute changes in the ground-state energy may cause excitation energy changes ($\delta\Delta_1$) that are larger by several orders of magnitude. However, for them to have a sizable effect on the orbital angular moment $\langle L_x\rangle$ and related parameters it is essential that ϕ^0 is near the inflection point of the $\langle L_x\rangle$ versus ϕ curve (Figure 7). Away from the inflection point, the relative change $\delta\Delta_1/\Delta_1$ is normally too small to give detectable changes in $\langle L_x\rangle$-dependent parameters because either Δ_1 is large (right of the inflection point) or $\delta\Delta_1$ is small because both the Δ_1 versus ϕ and $\langle L_x\rangle$ versus ϕ plots approach minima (left of the inflection point).

4.5. Origin of Distortion ϕ. Distortion ϕ turns on the off-diagonal CF interaction between d_{yz} and d_{z^2}, resulting in energy levels for the ground and excited state that are decreasing and increasing functions of ϕ, respectively.[20] Since CF theory is incomplete, in the sense that it does not include distortion-limiting interactions such as the steric repulsions between the ligands, it is an inadequate tool for making quantitative structure predictions. For this reason, we have resorted to DFT for the study of molecular conformation and potential energy surfaces. The optimized geometry for the truncated model (see Supporting Information) gives $\phi \neq 0°$, consistent with the notion that the distortion is an intrinsic property of the structure and not the result of external forces. However, the value calculated for ϕ ($\sim$20°) is larger than observed in the crystal structure because torsion ϕ in the truncated model is not hindered by bulky phenyl groups as in the case of the unabridged complex. The presence of a steric effect on ϕ is corroborated by the geometry optimization for the complete structure, which yields a considerably smaller torsion angle, $\phi \approx 0°$. Although we have not yet fully understood the origin of the failure to predict the observed value for ϕ, a preliminary analysis suggests that the distortion in the DFT calculation of the unabridged model is quenched by computationally overestimating the energy gap between d_{yz} and d_{z^2}.

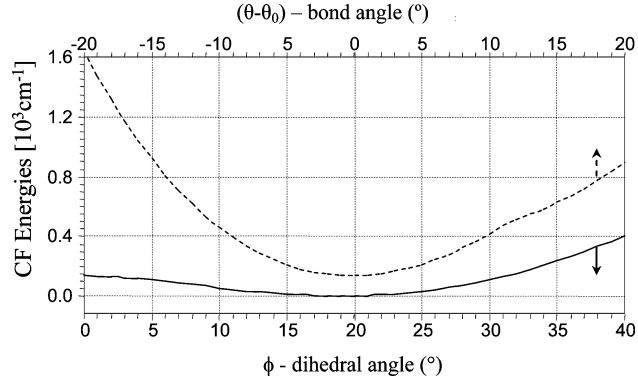

Figure 11. Relative SCF energies of truncated model vs ϕ for $\theta = \theta_0$ fixed (solid line) and vs θ for $\phi = 0°$ fixed (dashed line); $\theta_0 = 110.2°$. The energy of the dashed curve at the minimum is equal to the energy of the solid curve at the origin. The structure has C_{2v} point group symmetry for $\phi = 0°$ and C_2 symmetry otherwise.

4.6. Distribution in θ In the previous sections the torsion angle ϕ was singled out as the internal coordinate responsible for the distribution in A_x. In principle, any structural variable ξ may contribute to the width of the distribution. Using the ξ analogues of eqs 9a–d, the standard deviation of P_A generated by ξ can be written as

$$\sigma_{A,\xi} = \left[\frac{1}{4}P\left(\frac{d\langle L_x\rangle}{d\Delta_1}\right)_{\Delta_1^0}\right]\left(\frac{d\Delta_1}{d\xi}\right)_{\xi^0}\frac{1}{K_\xi}\sigma_f \tag{15}$$

where ξ^0 and K_ξ are, respectively, the equilibrium value and force constant for ξ. The expression for $\sigma_{A,\xi}$ depends on four factors. The first factor (in square brackets) is independent of ξ, the second and third ones measure the intrinsic propensity of coordinate ξ to disperse the value of A_x, and the fourth factor (σ_f) is the standard deviation of the random force acting on ξ. Equation 15 shows that a large tangent $d\Delta_1/d\xi$ and a small force constant K_ξ amplify σ_f to yield a large value for $\sigma_{A,\xi}$.

The relative magnitude of $\sigma_{A,\phi}$ and $\sigma_{A,\theta}$ has been estimated as follows. Using the CF level diagrams for Δ_1 versus ϕ and θ (Figure 8) we obtained the derivatives $(d\Delta_1/d\phi)_{10°} = 175\ cm^{-1}$/degree and $(d\Delta_1/d\theta)_{96°} = 18\ cm^{-1}$/degree. The force constants were obtained from DFT energy scans along ϕ and θ. The resulting potential energy surfaces are shown in Figure 11 and give,[21] upon parabolic fitting, the force constants $K_\phi = 0.78\ cm^{-1}/(deg)^2$ and $K_\theta = 3.02\ cm^{-1}/(deg)^2$. The value of σ_f in eq 15 depends on the nature of coordinate ξ, but since we have no knowledge about the specifics of the random forces, we assume that this quantity is equal for ϕ and θ. By substituting these values in eq 15 we obtain for $\sigma_{A,\phi}$ a value that is about forty times larger than the value for $\sigma_{A,\theta}$, supporting the idea that the distribution in A_x results predominantly from a distribution in ϕ.

Figure 12 summarizes the discussion. The figures show a contour plot of the potential energy surface for the ground state (right) together with a contour plot of $\langle L_x\rangle$ (left) as a

(19) The equilibrium geometry for an excited state is generally different from the ground state geometry.

(20) In Figure 8, where the ground-state energy is defined as the origin of the energy scale, the increasing "repulsion" between the two levels gives rise to a steady increase of Δ_1.

(21) The two-dimensional potential energy surface is presented in Figure 12.

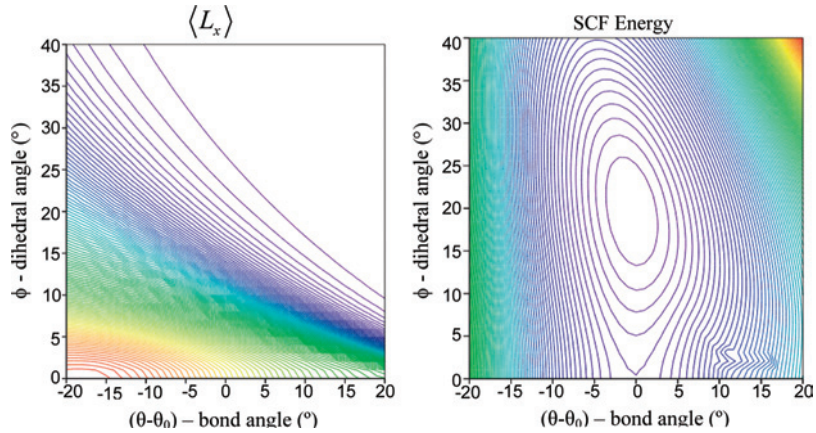

Figure 12. Left: contour plot of $\langle L_x \rangle$ as a function of $(\theta - \theta_0)$ (change in bond angle) and of ϕ (dihedral angle) as determined from the CF calculations for point charge model used. The $\langle L_x \rangle$ plot is color coded such that bright red corresponds to $\langle L_x \rangle = -1.92$ (lower left corner) and deep blue to $\langle L_x \rangle = -0.02$ (upper right region). Right: contour plot of the DFT ground-state energy for **1** as a function of $(\theta - \theta_0)$ and ϕ. The energy plot is color coded with bright red corresponding to 2700 cm^{-1} (upper right corner) and deep blue to 27 cm^{-1} (central region).

function of the changes in the bite angle and dihedral angle. The rate at which the equi-$\langle L_x \rangle$ lines are crossed as a function of ϕ (θ fixed) is greater than as a function of θ (ϕ fixed). This fact in combination with the relative shallowness of the potential for ϕ show that of the two angles $\langle L_x \rangle$ is most susceptible to changes in ϕ.

5. Conclusions

The change in the coordination of the high-spin Fe^{II} site from three-coordinate planar in L′$FeCl_2$ to quasi tetrahedral in $LFeCl_2Li(THF)_2$ increases the CF splitting between the lowest two 3d orbital states and reduces the spin−orbit mixing between them. This change leads to reductions in both the ZFS of the $S = 2$ ground manifold and the orbital term, $A_{L,x} > 0$. The orbital term, which gives by far the largest contribution to the magnetic hyperfine field in the three-coordinate species, cancels almost completely against the Fermi contact term, $A_{FC,x} < 0$, in the case of the four-coordinate complex. The resulting decrease in $A_x \approx A_{L,x} + A_{FC,x}$ entails that minor changes in $A_{L,x}$ have a large relative effect on this quantity. The impact of A_x on the Mössbauer spectra is particularly large because the molecular magnetization axis in **1** is directed along x (A_x is multiplied by a large spin expectation value). Thus, complex **1** presents ideal conditions for detecting distributions in A_x by means of Mössbauer spectroscopy. The experimental results section shows that it is indeed possible to observe the spectral manifestations of a distribution in A_x. In our search for the structural origin of this distribution we have identified the torsion angle ϕ (Figure 6) as the most likely candidate, based on the following considerations: (i) ϕ is "soft", that is, distortions along this coordinate can be made at low energy cost, (ii) ϕ couples effectively to excitation energy Δ_1 (Figure 8) which occurs in the denominator of the expression for $A_{L,x}$ (eq 7c), and (iii) at $\phi \approx 10°$ the system is in the intermediate spin−orbit coupling regime where $\langle L_x \rangle$ (Figure 7) and consequently $A_{L,x}$ are steep functions of ϕ. The observed spread in A_x ($\sigma_A \approx 1-2$ T) can be generated by subdegree distortions ($\sigma_\phi \approx 0.4-0.7°$) of the structure that represent sub-wavenumber perturbations of the ground-state energy.

One of the lessons learned in the course of the present study is that the appearance of substantial distributions in the spin Hamiltonian parameters does not necessarily signal substantial disorder. In some instances, as described here, some spin Hamiltonian parameters are delicately sensitive to minute structural changes.

Acknowledgment. This work was supported by NSF Grant MCB-0424494 (E.M.) and NIH Grant R01 GM65313 (P.L.H.).

Supporting Information Available: (i) Cartoons of the crystallographic structures of the two complexes present in the unit cell of the crystal form with space group $Pna2_1$. (ii) DFT results for three structural models for complex **1**, including relative energies, metric data, and Mössbauer parameters. (iii) Brief description of the crystal-field model and the crystal-field energies and states for the model with C_{2v} symmetry. (iv) Schemes with cartoons of the lowest two 3d orbitals in $LFe^{II}Cl$ and $LFe^{II}(\mu\text{-}Cl)_2Li(THF)$. This material is available free of charge via the Internet at http://pubs.acs.org.

IC8004568